Low-Symmetry 2D *t*-InTe for Polarization-Sensitive UV-Vis-NIR Photodetection

Nan Zhou, Ziwei Dang, Haoran Li, Zongdong Sun, Shijie Deng, Junhao Li, Xiaobo Li, Xiaoxia Bai, Yong Xie,* Liang Li, and Tianyou Zhai*

Polarization-sensitive photodetection grounded on low-symmetry 2D materials has immense potential in improving detection accuracy, realizing intelligent detection, and enabling multidimensional visual perception, which has promising application prospects in bio-identification, optical communications, near-infrared imaging, radar, military, and security. However, the majority of the reported polarized photodetection are limited by UV–vis response range and low anisotropic photoresponsivity factor, limiting the achievement of high-performance anisotropic photodetection. Herein, 2D *t*-InTe crystal is introduced into anisotropic systems and developed to realize broadband-response and high-anisotropy-ratio polarized photodetection. Stemming from its narrow band gap and intrinsic low-symmetry lattice characteristic, 2D *t*-InTe-based photodetector exhibits a UV–vis–NIR broadband photoresponse and significant photoresponsivity anisotropy behavior, with an exceptional in-plane anisotropic factor of 1.81@808 nm laser, surpassing the performance of most reported 2D counterparts. This work expounds the anisotropic structure-activity relationship of 2D *t*-InTe crystal, and identifies 2D *t*-InTe as a prospective candidate for high-performance polarization-sensitive optoelectronics, laying the foundation for future multifunctional device applications.

1. Introduction

Polarization-sensitive photodetection grounded on low-symmetry 2D materials has immense potential for improving detection accuracy, realizing intelligent detection, and enabling multidimensional visual perception, due to the ability of detecting a larger phase difference to small changes on the surface of the detected target, and changing the intensity difference between the scattering light of interfering particles and the reflected light of the target, which has promising application prospects in bio-identification, optical communications, near-infrared imaging, radar, military, and security.[1] Recently, growing anisotropic members such as, 2D ZrS_3,[2] $SiAs$,[3] SiP_2,[4] KNb_3O_8,[5] and violet phosphorus,[6] have been investigated for polarized photodetection, but most of the above-reported photodetection were limited to the UV–vis response range, hindering their further integrated optical applications for broadband-response polarization detection.[7] Few in-plane anisotropic 2D materials, such as 2D $Sn^{II}Sn^{IV}S_3$,[8] and SnS,[9] are capable of detecting near-infrared light, but their low anisotropic photoresponsivity ratio greatly hinders the achievement of high-performance anisotropic optoelectronics. Therefore, exploring and developing novel low-symmetry 2D materials with suitable narrow-band gaps and high anisotropic photoresponsivity ratio will be rewarding for lifting the above restriction and realizing polarization-sensitive

N. Zhou, Z. Dang, H. Li, S. Deng, X. Li, X. Bai, Y. Xie
Shaanxi Joint Key Laboratory of Graphene, School of Advanced Materials and Nanotechnology
Xidian University
Xi'an 710126, P. R. China
E-mail: yxie@xidian.edu.cn
N. Zhou, X. Li
Guangzhou Institute of Technology
Xidian University
Guangzhou 710068, P. R. China

Z. Sun, T. Zhai
State Key Laboratory of Materials Processing and Die & Mould Technology, School of Materials Science and Engineering
Huazhong University of Science and Technology
Wuhan 430074, P. R. China
E-mail: zhaity@hust.edu.cn
J. Li
Institute of Information Sensing
Xidian University
Xi'an 710126, P. R. China
L. Li
Key Laboratory of Materials Physics, Anhui Key Laboratory of Nanomaterials and Nanotechnology, Institute of Solid State Physics, Hefei Institutes of Physical Science
Chinese Academy of Sciences
Hefei 230031, P. R. China
T. Zhai
Optics Valley Laboratory
Hubei 430074, P. R. China

**ADVANCED
SCIENCE NEWS**

www.advancedsciencenews.com

**NANO · MICRO
small**

www.small-journal.com

photodetection with broadband response and strong anisotropic sensitivity.

III-VI semiconductor tetragonal phase (*t*-) InTe stands out as an ideal candidate material to address the above challenge, due to the features of a relatively narrow band gap, and strong structure anisotropy derived from low-symmetry chain structure composed of $[Tl^{3+}(Te^{2-})_2]^{1-}$ and In^+.[10] However, compared with other counterparts, *t*-InTe has more sister materials with different element proportions, such as In_2Te_3, In_3Te_4, In_2Te_5, In_7Te_{10}, etc.[10d] and different phase structures with small conversion energy, involving face-centered cubic phase (*rs*-InTe), and body-centered cubic phase (*c*-InTe).[11] Due to the existence of this multiple proportions of component, polycrystalline phase, combined with non-layered crystal structure, the experimental exploration on polarized optoelectronics of 2D *t*-InTe was limited, impeding the study of high-performance anisotropic optoelectronics.
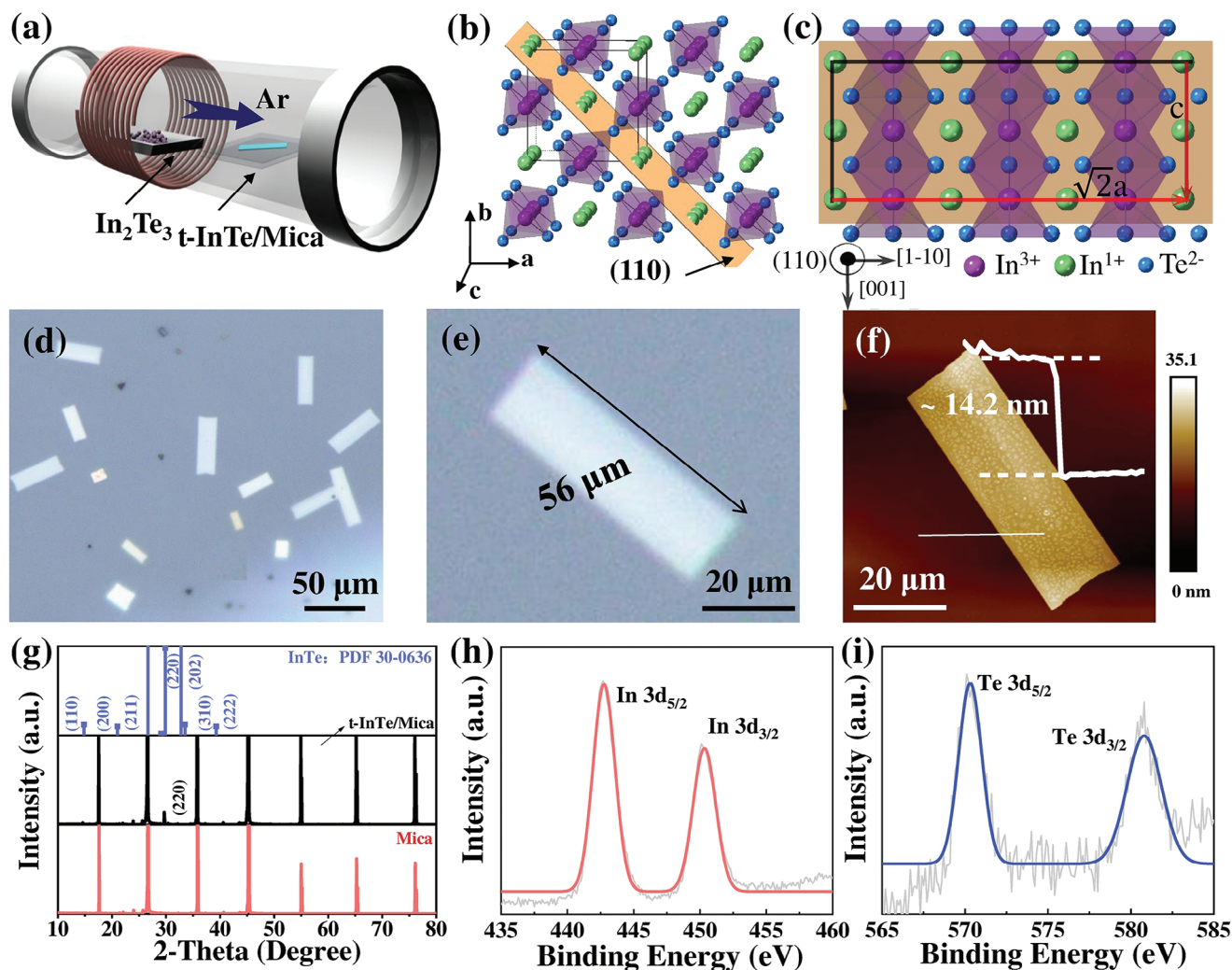
In this study, 2D *t*-InTe was introduced into anisotropic systems and developed to realize broadband-response and high-anisotropy-ratio polarization-sensitive photodetection. Large-area 2D *t*-InTe nanosheets were achieved firstly via low-pressure and space-confined chemical vapor deposition (CVD). Structural characterization demonstrated that the obtained products were tetragonal 2D *t*-InTe crystals with high crystalline quality. Impressively, originating from its narrow band gap (≈ 1.28 eV) and intrinsic low-symmetry crystal structure, 2D *t*-InTe-based photodetector exhibited a UV–vis–NIR photoresponse with outstanding near-infrared detection performance (photoresponsivity (R_λ) = 8.37 AW^{-1}, external quantum efficiency (EQE) = 1.28×10^3, and detectivity (D^*) = 2.68×10^{11} Jones @ 808 nm), and a significant photoresponsivity anisotropy behavior, with an exceptional anisotropic factor of 1.81 for 808 nm incident laser, superior to the performance of most 2D anisotropic counterparts. Moreover, polarization-resolved electrical transport measurement confirmed that 2D *t*-InTe also exhibited excellent anisotropic conductance and hole mobility, with high in-plane anisotropy factors of 1.74 and 3.22, respectively. Such distinctive broadband-response feature, excellent near-infrared detection performance, in combination with strong anisotropy in polarized photodetection, enable 2D *t*-InTe as a promising campaigner for high-performance polarization-sensitive optoelectronics.

2. Results and Discussion

Here, low-pressure, and space-confined CVD were used to achieve high-quality 2D *t*-InTe nanosheets, as the synthesis setup illustrated in **Figure 1a**. In_2Te_3 power was used as the precursor of the reaction, and two mica flakes for constructing the confined space were used as the substrate for collecting the products. Under the low-pressure environment and the transport of high purity Ar, In_2Te_3 vapor diffuses into the confined space, adsorbed, and incorporated on the mica substrate, and large-area 2D *t*-InTe nanosheets were obtained. Here, the low-pressure inert atmosphere helps to reduce the reaction temperature and improve the crystalline quality of the product (Figure S1, Supporting Information). The absence of dangling bonds on mica substrate can inhibit vertical growth and facilitate the horizontal growth of 2D products (Figure S2, Supporting Information).[12] The confined space contributes to reducing the nucleation density and reaction rate, further realizing the preparation of ultra-

thin 2D *t*-InTe flakes (Figure S3, Supporting Information). For an in-depth understanding of its structure, the detailed crystal structure diagram is shown in Figure 1b and Figure S4 (Supporting Information). As a typical III-VI semiconducting compound, *t*-InTe forms a body-centered tetragonal system, with a chained TlSe structure (space-group, $I4/mcm$ (D_{4h}[18])).[13] Furthermore, Indium (In) atoms occupy two different crystallography positions in the *t*-InTe lattice, including two mixed valences consisting of monovalent In$^+$ and trivalent In^{3+} ions. Monovalent In^{1+} ions are surrounded by eight tellurium ions Te^{2-}, whereas Te^{2-} surround trivalent In^{3+} ions tetrahedrally. Therefore, long negatively charged chains of atoms $[In^{3+}(Te^{2-})_2]^{1-}$ were formed along the *c*-axis, and In^{1+} ions were concentrated in the vicinity of negatively charged chains, which are kept together via weak interchain ionic interactions. The binary chained *t*-InTe was precisely denoted as $In^{1+}[In^{3+}(Te^{2-})_2]^{1-}$.[13,14] Moreover, the weak interchain bonds and strong intrachain ion-covalent bonds of *t*-InTe crystal were similar to the layered structure, contributing to the construction of parallel 2D plane plates with the *c*-axis as their orientation. Because of the tenuous connections between $(InTe_2)^-$ chains, the crystal may tend to grow/cleave along the plane of weakly bonded In$^+$ cations residing in the tunnels, such as along the (110) plane (Figure 1c),[15] strong interaction along the *c*-axis and weakly bounded chains along [1–10] give rise to considerable in-plane anisotropic physical properties in (110) crystal plane. Thus, significant differences in the structure and chemical composition between intrachain and interchain lead to the low symmetry and high anisotropy of 2D *t*-InTe.

Owing to the above-mentioned tetragonal crystal phase, as-synthesized 2D *t*-InTe nanosheets show characteristic rectangular shapes on mica substrates (Figure 1d), indicating the preferential growth orientation of 2D *t*-InTe caused by its anisotropic crystal structure. By optimizing synthesis parameters, the lateral dimension of the obtained crystal can be up to 56 µm (Figure 1e), and the atomically sharp edges, relatively smooth surfaces, and thickness as thin as 14.2 nm were also realized, identified by atomic force microscopy (AFM) (Figure 1f). The above sample characteristics facilitate subsequent device preparation. Some other 2D *t*-InTe nanosheets with different thicknesses were also demonstrated in Figure S5 (Supporting Information), laying a foundation for the discussion of thickness-dependent optical properties later. Additionally, X-ray diffraction (XRD) patterns were collected to further determine the crystal structure and crystal face of as-synthesized 2D *t*-InTe crystal (Figure 1g). Excluding peaks of mica substrate, one prominent peak at 29.8 degrees was confirmed, which was identified as the (220) crystal plane of tetragonal phase InTe, verifying the high-pure phase of the obtained flakes. Simultaneously, (110) crystal plane was identified as the preferred orientation growth plane,[16] in agreement with early studies.[15] Besides, X-ray photoelectron spectroscopy (XPS) was implemented on the as-prepared crystal to further characterize the elemental binding energies, as shown in Figure 1h,i. In 3d$_{5/2}$ and In 3d$_{3/2}$ states are responsible for the peaks at 442.7 eV and 450.4 eV, and Te 3d$_{5/2}$ and Te 3d$_{3/2}$ states are responsible for the peaks at 570.3 eV and 580.8 eV, respectively, consistent with previously reported results.[17] No other evident oxidation peaks support the comparable chemical stability of the obtained 2D crystal.
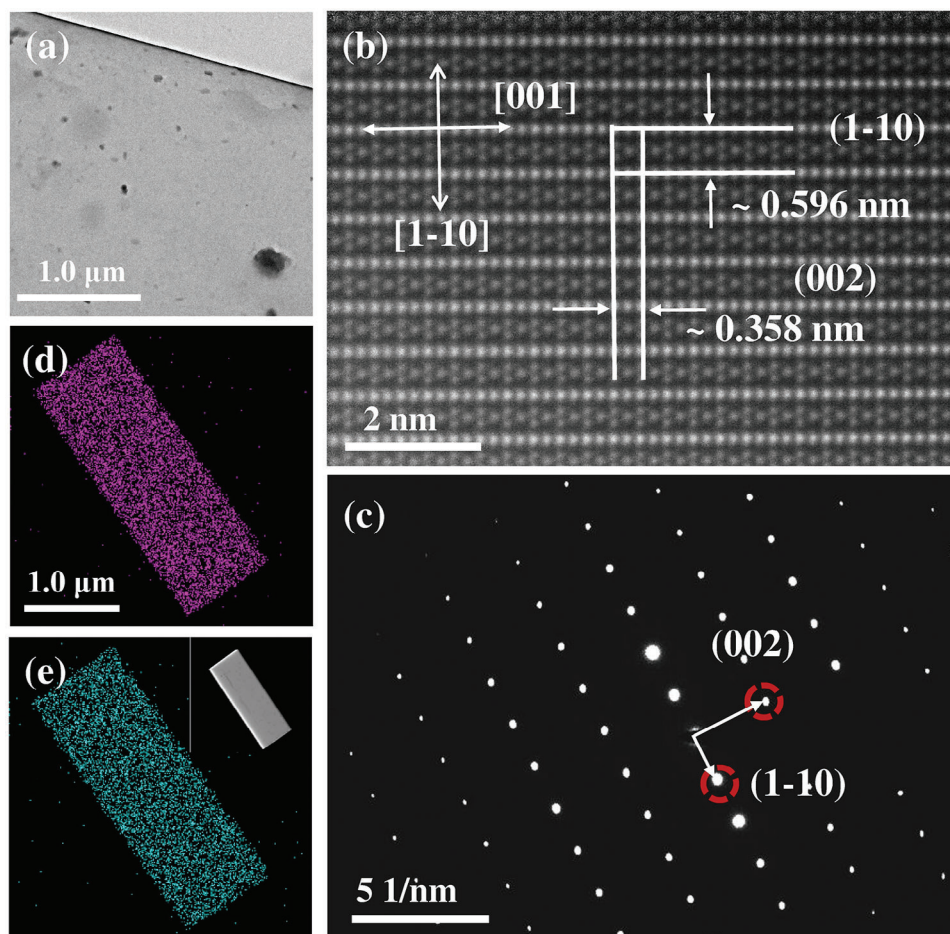
ADVANCED
SCIENCE NEWS
www.advancedsciencenews.com

NANO · MICRO
small
www.small-journal.com

Figure 1. Synthesis and characterizations of 2D t-InTe flakes. a) Schematic diagram of preparing 2D t-InTe by low-pressure and space-confined CVD. b) Crystal structure of t-InTe flakes, and the preferential growth plane or cleavage plane (110) (orange color). c) Atomic arrangement diagram of crystal plane (110), with strong intrachain covalent bond along [001] and weak interchain interaction along [1–10], implying a high in-plane anisotropy in (110) crystal surface. d, e) Optical image of as-synthesized 2D t-InTe flakes, and a characteristic flake with a marked horizontal dimension of 56 μm. f) A typical AFM image with the corresponding height profile. g) XRD patterns of 2D t-InTe flakes on mica (black line), the normal XRD patterns of mica (red line), and t-InTe crystal (blue line). XPS characterization of h) In 3d and i) Te 3d states.

To further investigate the low-symmetry structure and microstructure of 2D t-InTe in detail, Transmission electron microscopy (TEM) characterizations were carried out. TEM image at low magnification displays the sharp long edge of a 2D t-InTe rectangular flake, as displayed in **Figure 2a**. Aberration-corrected transmission electron microscope (STEM) image and high-resolution TEM (HRTEM) picture both present an obvious chain structure and lattice fringes (Figure 2b; Figure S6, Supporting Information), by further measuring the lattice spacing, the short edge along [1-10] and the long edge along c-axes were determined, respectively. The selected-area electron diffraction (SAED) image collected from the edge of the t-InTe flake presents a clear rectangular lattice (Figure 2c), verifying the tetragonal crystal system and single-crystal property. Based on the marked (1-10) and (002) crystal planes, and the rectangular SADE pattern, [110] zone axis and (110) growth plane of 2D t-InTe were identi-

fied, consistent with the XRD results and the previously reported optimal cleaving surface.[15,18] Subsequently, Energy-dispersive X-ray (EDX) analysis was adopted to determine the composition, verifying that the atomic ratio of constituent elements of In and Te was 1:1 (Figure S7, Supporting Information), and In and Te elements were distributed uniformly throughout the film (Figure 2d,e), demonstrated by EDX mapping. The EDX results proved the synthesized sample is InTe with high quality. All the above plan-view TEM results provide conclusive evidence for the low-symmetry crystal structure of as-prepared 2D t-InTe, contributing to further investigating in-plane anisotropic electronic and optoelectronic properties. Moreover, to figure out the cross-sectional crystal structure of 2D t-InTe, aberration-corrected TEM characterization was carried out (Figure S8, Supporting Information). First, a thinned specimen (Figure S8a, Supporting Information) was extracted from 2D t-InTe via a focused ion beam

**ADVANCED
SCIENCE NEWS**

www.advancedsciencenews.com

NANO · MICRO

small

www.small-journal.com

Figure 2. Composition and structure characterizations of as-prepared 2D *t*-InTe flake. a) TEM image at low magnification, b) aberration-corrected STEM image, and c) the acquired SAED patterns of 2D *t*-InTe flake. EDX element mapping d) In and e) Te.
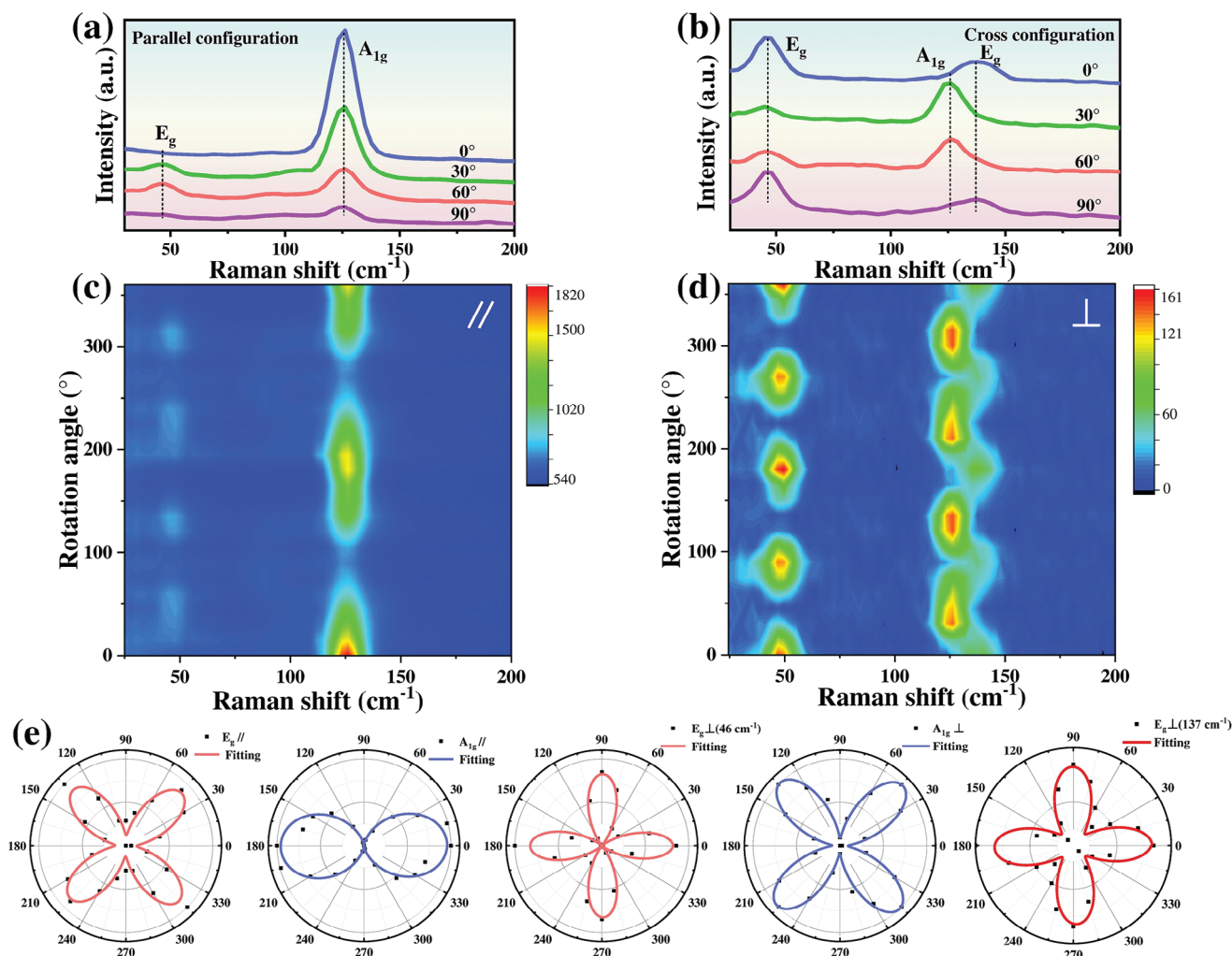
technique, whose long edge was parallel to the c-axis of 2D rectangular flakes. Then, a high angle annular dark field STEM image of cross section was collected by aberration-corrected TEM (Figure S8b, Supporting Information), in which the binary-chained repeating units confirmed quasi-layered structure along the growth direction, and the interlayer distance of the crystal face (110) was measured to be 0.592 nm, approximately consistent with XRD data. In addition, combined with the simulated cross-section atomic arrangement diagram obtained via CrystalMaker software (Figure S8c, Supporting Information), In^{+} cations, In^{3+} cations, and Te^{2-} anions were tagged on the STEM image. In addition, the structure information was also obtained by cross-section HRTEM image (Figure S8d, Supporting Information), which was consistent with the STEM results. These cross-section TEM results confirmed the quasi-layered structure, the distribution of cations and anions, and layer distance, and provided detailed structure information for novel 2D *t*-InTe.

To ascertain the composition of the obtained crystal, Raman spectra were collected based on 20.8-nm-thicked 2D *t*-InTe on mica substrate (Figure S9a, Supporting Information). When excited by a 633-nm laser, 2D *t*-InTe flakes showed three vibrational modes located at 85, 126, and 137 cm^{-1}, attributed to B_{1g}, A_{1g}, and E_g, respectively.[18] However, when the irradiated source was

changed to a 532-nm laser, 2D *t*-InTe flakes showed three different vibrational modes, including E_g (46 cm^{-1}), B_{1g} (90 cm^{-1}), and A_{1g} (126 cm^{-1}), which were consistent with the previously reported results.[19] Here, the weakening and shift of B_{1g} mode, the undetectability of E_g mode at 137 cm^{-1}, and the appearance of E_g mode at 46 cm^{-1} were probably attributed to that photon-phonon vibration with different intensities existed between excitation lasers with different wavelengths and 2D *t*-InTe crystal or the resonance enhancement of the crystal subpopulations with different vibrational frequencies.[20] Compared with 17 Raman active modes obtained by the reported theoretical calculations,[21] there are only 4 modes detected in our characterization, which may be derived from their low frequency or weak electron−phonon interactions.[22] In addition to irradiation sources, the influence of thickness on Raman spectra was also compared and investigated, as depicted in Figure S9b (Supporting Information). The intensity increased gradually with sample thickness and peak positions were almost the same for 14.2-nm, 21.8-nm, 27.2-nm, and 41.6-nm crystals, implying that Raman spectra did not shift appreciably with the thickness within the test range, similar to other III−VI group 2D materials.[23]

On account of the low-symmetric crystal structure, the prepared 2D *t*-InTe should possess strong in-plane anisotropic

Figure 3. ARPRS of 2D *t*-InTe flake. Polarized Raman spectra and the related contour maps under parallel (a, c) and perpendicular b, d) configurations. e) Raman intensities varying with rotation angle under two configurations for the typical E_g (46 cm^{-1}), A_{1g}, and E_g (137 cm^{-1}) Raman modes. Note: the experimental data were indicated by the black dots, and the fitted curves were represented by the red and blue lines.

optical properties. Therefore, angle-resolved polarized Raman spectroscopy (ARPRS) was performed to survey the anisotropy of phonon vibration modes under parallel and perpendicular backscattering configurations, based on a 20.8-nm-thicked 2D *t*-InTe flake. During the characterization, a linear polarizer was placed in the optical path between the sample and the Raman detector, and the corresponding Raman signals parallel or vertical to the polarization direction of the incident laser were recorded via the Raman detector. By rotating the sample from the orientation of the long edge at an interval of 30° (Figure S10, Supporting Information), the angle-resolved Raman peak can be observed with a variation period of 90° or 180° for maximum values (**Figure 3**a,b). However, the polarized peak positions were almost unchanged, consistent with those of the unpolarized Raman-scattering spectrum (Figure S11, Supporting Information). The polarized Raman intensity depending on rotation angles was further extracted and plotted in contour color mapping (Figure 3c,d), from which clear periodic changes with the rotation angle (0°−360°) for the intensity of the typical Raman vibration

modes were observed, except for the weak-signal B_{1g} mode, and the strong dependence on rotation angle demonstrated the high in-plane anisotropy of 2D *t*-InTe crystal. To more clearly represent the polarization of single vibration mode, polarized intensity polar plots were plotted (Figure 3e), in which the angle-dependent Raman vibration intensities were normalized, based on dividing them by the maximum intensity. From the polar plots, the detected Raman vibration modes with diverse anisotropy were clearly observed. Under parallel polarization configuration, E_g mode (46 cm^{-1}) exhibits a four-leaf pattern, with the maximum intensities at 45°, 135°, 225°, and 315°. At the same time, the A_{1g} mode (126 cm^{-1}) exhibits a different two-leaf layout with a 180° period, and the maximum intensities were located at 0° and 180°. Under perpendicular configuration, all three Raman vibration modes exhibit a four-leaf pattern, with the maximum intensity of E_g mode (46 cm^{-1} and 137 cm^{-1}) at the rotation angles of 0°, 90°, 180°, and 270°, and the maximum intensity of A_{1g} mode at the rotation angles of 45°, 135°, 225°, and 315°. In addition, we noted that due to the Raman modes at 46 cm^{-1} and 137 cm^{-1} both

**ADVANCED
SCIENCE NEWS**

www.advancedsciencenews.com

NANO · MICRO

small

www.small-journal.com

belonging to the E_g mode, their intensity patterns and rotation angles for the maximum intensity under perpendicular constructions were uniform. However, the Raman modes at 137 cm^{-1} under parallel constructions were not detected, related to the weak signal presented in this polarization configuration. Moreover, the aforementioned experimental phenomena reflect that the Raman intensity of different modes either reaches the minimum value or maximum value, as the polarized laser direction is consistent with the crystal orientation. Thus, the crystalline orientation of 2D t-InTe can be identified via ARPRS, and the phonon symmetry is crucial to understanding the anisotropy of Raman intensity.
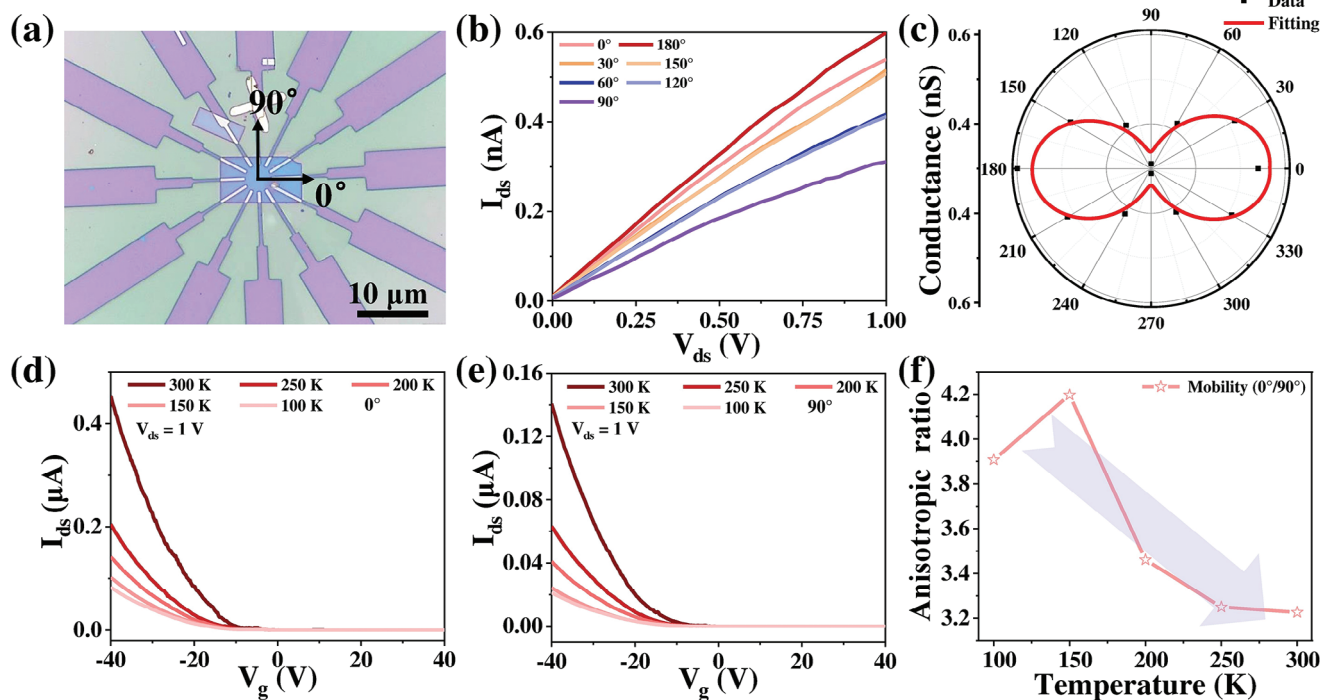
To understand deeply the anisotropy of phonon vibration modes, a quantitative analysis of polarized Raman intensities based on the classical Placzek was performed.[24] From equations (4) to (9) in the Supporting Information, it can be noticed that the pattern and period of each vibrational mode rely on the configuration and the Raman tensor. As shown in Figure 3e, by fitting the polarized Raman intensity via the Raman tensor, the fitting curves (pink and blue) correspond well with the experimental results (black dots) under parallel and perpendicular configurations. For the polar plots of E_g (46 cm^{-1}) mode, four-leaf patterns for the parallel configuration were rotated 45° clockwise and transformed into that for the cross configuration. For the polar plots of A_{1g} (126 cm^{-1}), two-leaf patterns under parallel configuration were converted into four-leaf patterns for the perpendicular configuration. Additionally, according to equation (4) in the Supporting Information, the direction of the primary axis was determined by the $\frac{|b|}{|a|}$ (a and b stand for tensor elements in the Raman tensor expression): if $\frac{|b|}{|a|} > 1$, the primary axis is along the x-direction.[22] The above ARPRS characterization confirmed that 2D t-InTe possesses strong in-plane anisotropy for phonon vibration modes.

As is reported, second-harmonic generation (SHG) was highly sensitive to structural configurations including lattice symmetry and defects such as vacancies, grain boundaries, etc.[25] Therefore, SHG not only can probe the symmetry properties of 2D materials but also can verify the external symmetry perturbations on them. Here, although 2D t-InTe crystals have a centrosymmetric lattice structure, strong SHG signals can be detected, which may be attributed to defects of 2D t-InTe crystals.[25a] These perturbations can effectively break the overall inversion symmetry of the system. Then, detailed SHG characterization was performed as follows, and the influence of key factors, such as incident laser wavelength, laser intensity, and sample thickness, on SHG was further explored.[26] Based on 14.2-nm 2D t-InTe flake, SHG intensity depending on the excitation wavelength was first investigated (Figure S12a, Supporting Information), which proved the broad spectral response varying from 780 to 960 nm for efficient and stable SHG signal. Grounded on the strongest response signal of all excitation wavelengths, an 840-nm incident laser was selected for further investigating the effect of excitation power on SHG intensity (Figure S12b, Supporting Information), and it can be observed that the SHG signals become stronger with increasing excitation power. Their dependence relationship was further fitted via the first-order perturbation theory, and the obtained fitting factor of 2.1 was consistent with the theoretical value (Figure S12c, Supporting Information).[27] Thickness-dependent SHG intensity confirmed SHG signals increased with

sample thickness from 14.2 to 41.6 nm (Figure S12d, Supporting Information), which may be attributed to the increase in stacking fault concentration. It also indicated that stacking faults here break the inversion symmetry structure regardless of the thickness of 2D t-InTe crystal, which ensured the stability of nonlinear frequency conversion efficiency under varying thicknesses, at least for the measured thickness range. The above results confirmed that 2D t-InTe crystal is an excellent optical-frequency-doubled carrier when appropriate defects are introduced.

To investigate the electrical anisotropy of 2D t-InTe crystal, angle-resolved electrical transport measurements were performed. As the optical image of the back-gate field effect transistor (FET) device displayed in **Figure 4**a, six pairs of electrodes were uniformly constructed on the same 2D t-InTe crystal with an interval of 30°, thus, the transistor channels have the same channel size. In addition, parallel to the c-axis was regarded as 0°, consistent with the rotation angle defined by ARPRS (Figure S10, Supporting Information). At a gate voltage of 0 V, the characteristic source-drain current-voltage (I_{ds} -V_{ds}) curves of each pair of electrodes exhibit an approximate ohmic contact, due to the small barrier difference,[28] and the current I_{ds} presents an obvious angle dependence (Figure 4b). To further confirm the above results, the conductance extracted from I_{ds}-V_{ds} curves were plotted in polar coordinates (Figure 4c) and further fitted by the formula: $\sigma_\theta = \sigma_a \cos^2\theta + \sigma_b \sin^2\theta$, where σ_a and σ_b represent conductance parallel to the c-axis and perpendicular to it, respectively, and the perfect fit confirmed the conductance anisotropy. The derived in-plane anisotropic ratio of the conductivity (σ_a/σ_b) was 1.74, slightly superior to comparable 2D materials like 2D PdSe$_2$ and Black Arsenic.[29]

To further quantitatively analyze these results, the temperature-dependent transfer characteristic curves along the c-axis and perpendicular to that were measured (Figure 4d,e), which verified p-type conduction characteristics, hole mobility of 0.48 cm^2 V^{-1} s^{-1} and a significant current on/off ratio of 2×10^5 parallel to the c-axis at room temperature. The above performance were comparable with or inferior to those of other reported 2D counterparts.[30] In addition, the mobility was also inferior to the reported predicted value because the obtained effective mobility was lower than the intrinsic free-carrier mobility, which may be derived from the existence of few charge traps such as charge impurities, dopants, and defects.[31] The undistinguished hole mobility may affect photodetection performance via reducing the transmission of photogenerated carriers, such as photocurrent, photoconductive gain, responsivity, response time, and detectivity, et al.[32] Further research on optimizing the film quality, adopting the high-k dielectric layer, and implementing packaging technology to obtain larger hole mobility is underway. It is reported that the mobility anisotropy arises from the anisotropic effective hole mass. Here, for 2D t-InTe, the reported effective hole mass along the chain direction is ten times larger than that of the perpendicular one, thus producing strong-anisotropy mobility.[33] Moreover, carrier mobility parallel to the c-axis (perpendicular to that) was improved from 0.089 to 0.48 cm^2 V^{-1} s^{-1} (from 0.023 to 0.15 cm^2 V^{-1} s^{-1}) with the temperature increasing from 100 K to 300 K (Figure S13, Supporting Information), confirming that the main scattering mechanism to limit mobility is charge impurity scattering.[34] However, the anisotropic hole mobility ratio ($\mu_{//}: \mu_\perp$) gradually decreases from

ADVANCED
SCIENCE NEWS

www.advancedsciencenews.com

NANO · MICRO
small

www.small-journal.com

Figure 4. Angle-dependent electrical transport characterizations of 2D *t*-InTe flakes. a) OM image of 2D *t*-InTe-based FET device with twelve electrodes at intervals of 30°, and the electrodes along the *c*-axis were taken as the 0° reference. b) Angle-resolved output characteristic curves at $V_g = 0$ V. c) Polar plots of conductance varying with angle. Transfer characteristic curves depending on temperature for the electrodes d) along the *c*-axis (0° direction) and e) perpendicular to it (90°direction). f) Temperature-dependent hole mobility ratios ($\mu_{//}$: $\mu_\perp$) along the *c*-axis and that perpendicular to it.
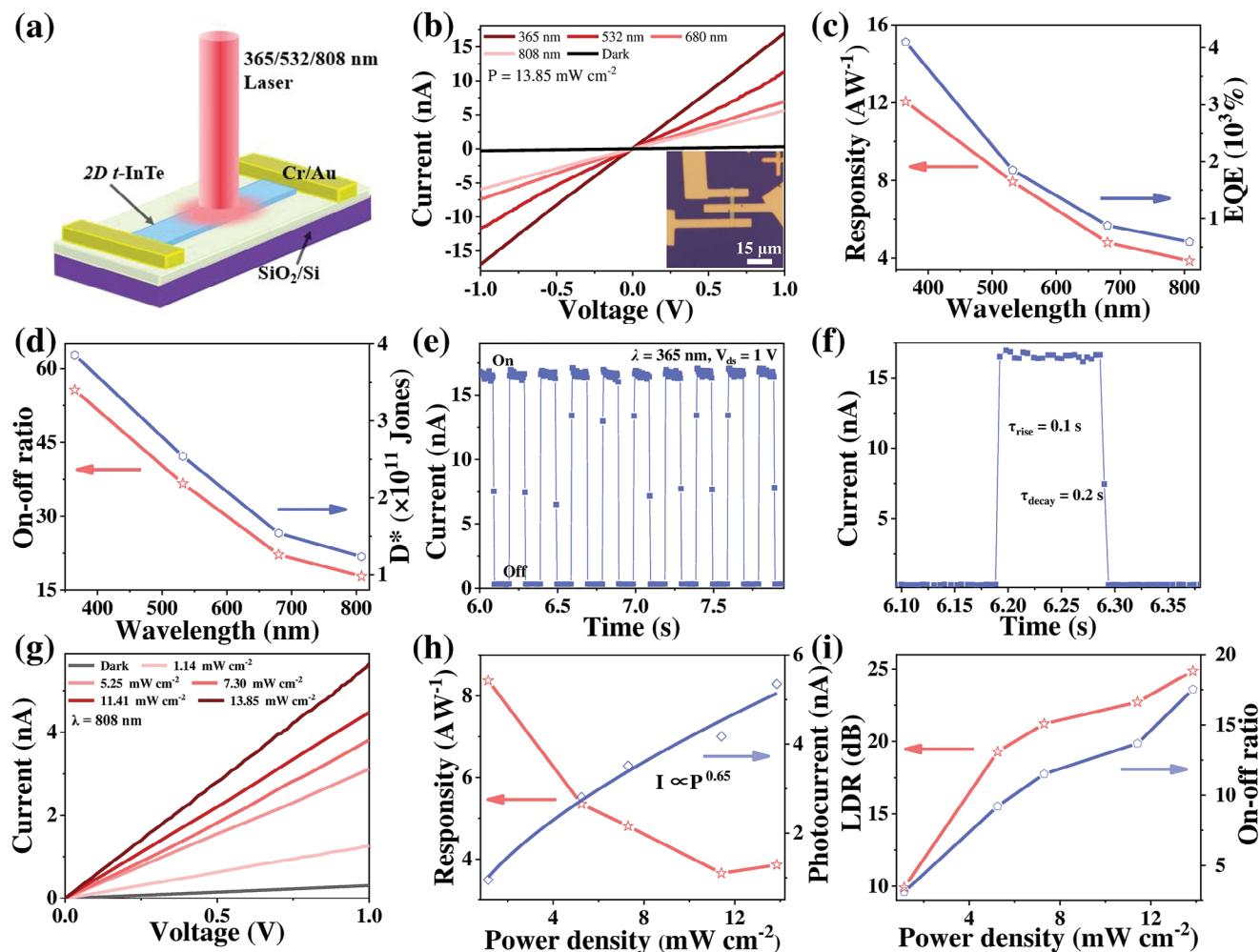
3.90 to 3.22 with increasing temperature (Figure 4f), which was attributed to the different reliance of the effective hole mass along diverse axes on temperature, and the large mobility ratio confirmed strong anisotropic electrical response, in contrast to other anisotropic 2D materials.[29b,35] Moreover, the adjustability of the hole mobility ratio was comparable with that of 2D BP flake.[36] Based on the strong-anisotropy electrical properties, the crystalline orientation of 2D *t*-InTe can also be identified via angle-resolved electrical transport measurements.

The narrow band gap property of 2D *t*-InTe encouraged us to explore its application in UV–vis–NIR photodetection,[10d–g] and photodetectors based on 2D *t*-InTe crystals were fabricated by standard microelectronic technology with Cr/Au (10/80 nm) metal contacts, as the device inset displayed in **Figure 5a**. Under 365-nm, 532-nm, 680-nm, and 808-nm laser illumination, 2D *t*-InTe-based photodetector demonstrated obvious photoresponse characteristics, demonstrating that 2D *t*-InTe nanosheets possess a UV–vis–NIR broadband photoresponse (Figure 5b). Here, the broadband photoresponse is consistent with the absorption spectra, from which the band gap of ≈ 1.28 eV was inferred, and the relatively weak super-bandgap absorption was probably related to a low density of shallow level and a low density of in-gap states in the crystal (Figure S14, Supporting Information).[37] R_λ, *EQE*, on-off ratio (I_{on}/I_{off}), and D^* were generally considered as the important indexes for assessing photoelectric conversion capability, sensitivity, and weak-optical-signal detection capability of photodetection,[38] which were extracted and discussed further. According to the formula of $R_\lambda = I_{ph}/PS$ (I_{ph} stands for photocurrent, *P* refers to the light power, and *S* is the active illuminated

area of ≈10 μm²) and $EQE = hcR_\lambda/e\lambda$ (*h*, *c*, *e*, and *λ* stands for the plank's constant, light velocity, electron charge, and excited wavelength, respectively), the maximum R_λ and *EQE* reached 12.05 A W⁻¹ and 4.09×10^3% for the 365-nm illumination (Figure 5c), superior to the performance of other 2D materials.[39] Based on the formula of $I_{on}/I_{off} = I_{ph}/I_{dark}$ (I_{dark} stands for dark current) and $D^* = R_\lambda S^{1/2}/(2eI_{dark})^{1/2}$, the extracted maximum on-off ratio and D^* were 55.6 and 3.85×10^{11} Jones (Figure 5d), respectively. Here, the unsatisfactory results may be related to its large dark current (0.30 nA) induced by strong conductivity,[10d,40] and could be reduced by further optimizing electrode contact or film quality. Moreover, with the redshift of incident wavelength, all the above four performance indexes gradually decreased, which confirmed that the photoelectric performance was strongly related to the incident wavelength, and dependent on light absorption fundamentally. The time-resolved photoresponse curve (*I-t*) of 2D *t*-InTe-based photodetector confirmed high cyclic stability and fast response speed (Figure 5e). By enlarging the cycle curve, the response time (0.1 s) and decay time (0.2 s) of the device were extracted (Figure 5f), which were faster than the reported photodetectors based on 2D PdSe₂ and RhI₃,[41] but slower than 2D InSiTe₃ and Sr₂Nb₃O₁₀.[7b,42] Here, this relatively general response time may be related to the defects-induced traps.[43] All the above results indicated that 2D *t*-InTe-based photodetector possesses relatively high photoelectric conversion capability.

To further investigate the near-infrared photodetection performance of 2D *t*-InTe, the *I-V* curves under 808-nm illumination with varying laser power from 1.14 to 13.85 mW cm⁻² were characterized in Figure 5g. The photocurrent rises progressively

**ADVANCED
SCIENCE NEWS**

www.advancedsciencenews.com
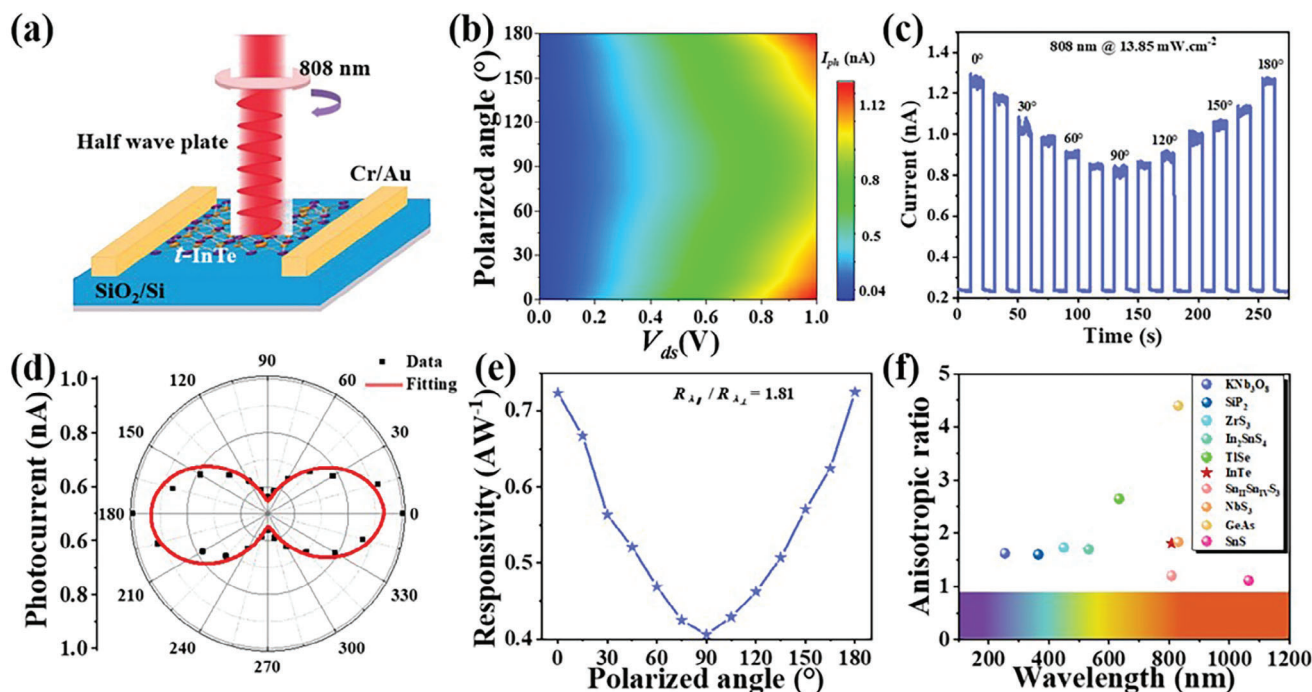
NANO · MICRO
small

www.small-journal.com

Figure 5. Photodetection performance of 2D t-InTe-based device. a) Schematic diagram of the photodetector. b) $I–V$ curves of the device upon irradiation of laser with diverse wavelengths and under dark. Inset: the OM image of the photodetector. c) Photocurrent and R_λ, d) EQE and $D*$ at different illumination wavelengths. e) $I–t$ cyclic curve of the photodetector upon 365-nm illumination. f) The corresponding transient response curve. g) $I–V$ curves for an 808 nm incident laser with different power densities. h) R_λ and photocurrent depending on diverse power densities, and the acquired fitting curve. i) On-off ratio and LDR versus varying light intensity.

with the enhancing laser power, and the relationship between them was fitted by the formula: $I_{ph} \propto P^\theta$ (θ is a fitting coefficient, $0<\theta<1$, P stands for irradiated laser power), as displayed in Figure 5h. The fitting factor of 0.65 confirmed the sublinear behavior, which was attributed to the defects and adsorbates at the t-InTe/substrate interface and on the t-InTe surface, suggesting that the photocurrent was primarily determined via the photoconductive mechanism.[44] The R_λ, EQE, and $D*$ all decrease with the enhancing light intensity, and the R_λ, EQE, and $D*$ were up to 8.37 AW^{-1}, 1.28×10^3%, and 2.68×10^{11} Jones for the low power density of 1.14 mW cm^{-2} (Figure 5g; Figure S15, Supporting Information), confirming that 2D t-InTe-based device responds well to weak light. The on−off ratio and photosensitivity linear dynamic range ($LDR = 20 \log (I_{ph}/I_{dark})$) varying with laser power were summarized in Figure 5i, and the on−off ratio and LDR were calculated to be 3.13 and 9.91 dB for 808 nm@1.14 mW cm^{-2}, and 17.53 and 24.87 dB for 808 nm@13.85 mW cm^{-2}. The LDR here is hopefully approaching that of presently used InGaAs

photodetectors (66 dB) for further device optimization, demonstrating that 2D t-InTe has vast potential in next-generation optoelectronic devices.[45] Here, the near-infrared photodetection performance of 2D t-InTe was comparable to or exceeded that of the majority of the reported near-infrared photodetectors, such as 2D Te and NbS (Table S1, Supporting Information),[46] derived from its relatively superior crystal quality and intrinsic strong light-material interaction.

Grounded on the above excellent near-infrared photodetection performance and inherent in-plane anisotropic structure characteristics, the linear dichroism of 2D t-InTe was further explored by characterizing polarization-dependent photodetection with linearly polarized near-infrared laser as irradiation source, as the diagram of photodetector shown in **Figure 6a**. The electrodes were fabricated at two ends of the long edge, and the directions of polarized light parallel to the long edge and the short edge were defined as 0 and 90°, respectively. Polarization-dependent photocurrent contour map of the photodetector upon 808 nm laser

**ADVANCED
SCIENCE NEWS**

www.advancedsciencenews.com

NANO · MICRO

small

www.small-journal.com

Figure 6. Polarization-sensitive photodetection performance of 2D *t*-InTe-based device. a) The schematic of polarization-sensitive 2D *t*-InTe-based photodetector. b) Angle-reliant photocurrent at varying V_{ds}, with polarized laser along the *c*-axis as 0° reference. c) polarization angle-dependent *I*−*t* curves. d) Normalized angle-resolved photocurrent polar plot. e) polarization-dependent responsivity, with the ratio between the responsivity parallel to the *c*-axis and perpendicular to that of 1.81. f) Comparison of the anisotropic ratio of photocurrent and response wavelength with other reported 2D and 1D materials, involving KNb_3O_8,[5] SiP_2,[4] ZrS_3,[2] In_2SnS_4,[48] TlSe,[22] $Sn^{II}Sn^{IV}S_3$,[8] NbS_3,[46b] GeAs,[49] and SnS.[9]

irradiation confirmed that the polarized photocurrent strongly relies on the bias voltage and rotation angle (Figure 6b). By adjusting the switching status of the laser and the rotation angle through the half-wave plate, the dynamic photoresponse of the photodetector under irradiation with different polarization angles was recorded (Figure 6c). The current under laser illumination displays a periodic variation with the rotation angle between the highest value and the lowest value, with the maximum along the *c*-axis and the minimum perpendicular to it. The extracted polarized photocurrent and the rotation angle were drawn in the polar coordinate plot (Figure 6d), and the experimental data can be fitted perfectly by the formula $I_{ph\theta} = I_{pha} \cos^2(\varphi) + I_{phb} \sin^2(\varphi)$, with the anisotropic factor of photocurrent as high as 1.81, consistent with the anisotropic factor of responsivity shown in Figure 6e. Here, the ratio exceeds that of the latest reported 1D KNb_3O_8 and 2D $Sn^{II}Sn^{IV}S_3$,[5,8] which demonstrated that 2D *t*-InTe flake has potential application in polarized optoelectronic devices. The high anisotropic photoresponsivity factor of 2D *t*-InTe nanosheet was derived from the greater light absorption parallel to the *c*-axis than perpendicular to it. In fact, the light absorption of photodetectors is mainly caused by the inter-band transition of electrons, also known as "inter-band absorption". Therefore, the interband absorption of 2D *t*-InTe is anisotropic. According to the fermi gold rule, the interband absorption is directly proportional to the joint density of states of the conduction band and valence band, and the transition probability, and the latter is closely related to the band structure of the material. In other words, its electron band structure is also anisotropic.[47] This is

another potential physical mechanism for high-anisotropy-ratio responsivity of 2D *t*-InTe, in addition to low-symmetry crystal structure. In addition, the response range and anisotropy ratio of the reported major polarized photodetectors have been listed in Figure 6f, from which the majority of polarized photodetectors were limited to the ultraviolet or UV–vis response range, and 2D *t*-InTe based device verified excellent polarization-sensitive near-infrared photodetection performance with high anisotropic ratio. Moreover, the 2D *t*-InTe-based device confirmed broadband photorespose range varying from 365 to 808 nm, proving that 2D *t*-InTe has potential application in high-performance polarized optoelectronic devices with broadband photoresponse.

3. Conclusion

In summary, a polarization-sensitive photodetection with broadband response and high anisotropic photoresponsivity ratio based on low-symmetry 2D t-InTe has been achieved. Large-scale 2D t-InTe nanosheets were obtained firstly via low-pressure and space-confined CVD. By precisely regulating pressure, 2D t-InTe nanosheets with a large horizontal size (56 μm) and a thinner thickness (≈ 14.2 nm) were obtained on mica substrate, and their tetragonal phase structure and high crystalline quality were confirmed by TEM characterization. Owing to its narrow band gap (≈ 1.28 eV) and low-symmetry crystal structure, 2D t-InTe-based photodetector presents a UV–vis–NIR broadband photoresponse with excellent near-infrared photodetection performance, and a strong anisotropic photoresponsivity with a high-anisotropy

factor of 1.81 for 808 nm incident laser. Furthermore, 2D *t*-InTe-based FET demonstrated strong anisotropic conductance and hole mobility by polarization-resolved electrical transport measurement, with high in-plane anisotropy factors of 1.74 and 3.22. Our work confirmed that 2D *t*-InTe is a promising candidate for high-performance broadband-response polarization-sensitive optoelectronics, paving the way for future multifunctional device applications.

4. Experimental Section

Synthesis: 2D *t*-InTe flakes were prepared via low-pressure and space-confined CVD method. The detailed preparation process was as follows: the In_2Te_3 power was taken as the precursor of the reaction and was set in the center of the heat source, and mica was used for the substrate of collected products and was placed downstream of the tube furnace. First, the furnace was preheated to 800°C and maintained for 10 minutes. Under appropriate low-pressure and 150 sccm Ar gas, the In_2Te_3 source was transported to the mica substrate and produced a decomposition reaction. Then, the furnace cooled down naturally, and 2D *t*-InTe flakes will be obtained on the mica substrates.

Characterization: The morphology of 2D *t*-InTe was characterized via an optical microscope (BX51, OLMPUS). The cross information was analyzed via AFM (Dimension Icon, Bruker). The components were identified by XRD (D8 VENTURE, Bruker), and XPS (ESCALAB 250, Thermo Fisher). The microstructure was studied via TEM (Tecnai G2 F30, FEI) and aberration-corrected TEM (Titan Cubed Themis G2 300). The polarized Raman spectra were analyzed via a Raman system (Alpha 300RS+, WITec). SHG signals were obtained with the help of a femtosecond laser (140 fs, 80 MHz).

Device Fabrication and Measurements: 2D *t*-InTe nanosheets were transferred onto a 300 nm SiO_2/Si substrate by PMMA-assisted transfer technology. Then, the electrodes were patterned via electron beam lithography and were produced via thermal evaporation. The FET devices use the heavily doped SiO_2 as the dielectric layer, and the electrical transport performance and photoelectric performance were performed on a probe station (TTPX, Lakeshore) and semiconductor analyzer (4200SCS, Keithley). The angle-resolved electrical transport and photodetection were characterized with the help of a half-wave plate and a polarizer.

Supporting Information

Supporting Information is available from the Wiley Online Library or from the author.

Acknowledgements

Conflict of Interest

The authors declare no conflict of interest.

Data Availability Statement

The data that support the findings of this study are available from the corresponding author upon reasonable request.

[1] a) L. Li, W. Han, L. Pi, P. Niu, J. Han, C. Wang, B. Su, H. Li, J. Xiong, Y. Bando, T. Zhai, *InfoMat* **2019**, *1*, 54; b) H. Y. Hou, S. Tian, H. R. Ge, J. D. Chen, Y. Q. Li, J. X. Tang, *Adv. Funct. Mater.* **2022**, *32*, 2209324; c) W. Xin, W. Zhong, Y. Shi, Y. Shi, J. Jing, T. Xu, J. Guo, W. Liu, Y. Li, Z. Liang, X. Xin, J. Cheng, W. Hu, H. Xu, Y. Liu, *Adv. Mater.* **2024**, *36*, 2306772; d) D. Wu, Y. Xu, H. Zhou, X. Feng, J. Zhang, X. Pan, Z. Gao, R. Wang, G. Ma, L. Tao, H. Wang, J. Duan, H. Wan, J. Zhang, L. Shen, H. Wang, *InfoMat* **2022**, *4*, e12320; e) H. Song, Y. Zhao, E. Turner, Y. Wu, Y. Li, M. Wu, G. Feng, H. Li, T. Zhai, *InfoMat* **2023**, *5*, e12397.

[2] X. Wang, K. Wu, M. Blei, Y. Wang, L. Pan, K. Zhao, C. Shan, M. Lei, Y. Cui, B. Chen, *Adv. Electron. Mater.* **2019**, *5*, 1900419.

[3] D. Kim, K. Park, J. H. Lee, I. S. Kwon, I. H. Kwak, J. Park, *Small* **2021**, *17*, 2006310.

[4] Z. Wang, P. Luo, B. Han, X. Zhang, S. Zhao, S. Wang, X. Chen, L. Wei, S. Yang, X. Zhou, *ACS Nano* **2021**, *15*, 20442.

[5] Y. Ping, H. Long, H. Liu, C. Chen, N. Zhang, H. Jing, J. Lu, Y. Zhao, Z. Yang, W. Li, F. Ma, X. Fang, Z. Wei, H. Xu, *Adv. Funct. Mater.* **2022**, *32*, 2111673.

[6] W. Chen, A. Chen, R. Zhang, J. Zeng, L. Zhang, M. Gu, C. Wang, M. Huang, Y. Guo, H. Duan, C. Hu, W. Shen, B. Niu, K. Watanabe, T. Taniguchi, J. Zhang, J. Li, X. Cai, G. Liu, *Nano Lett.* **2023**, *23*, 10821.

[7] a) R. Bai, T. Xiong, J. Zhou, Y.-Y. Liu, W. Shen, C. Hu, F. Yan, K. Wang, D. Wei, J. Li, J. Yang, Z. Wei, *InfoMat* **2021**, *4*, 12258; b) J. Chen, L. Li, P. Gong, H. Zhang, S. Yin, M. Li, L. Wu, W. Gao, M. Long, L. Shan, F. Yan, G. Li, *ACS Nano* **2022**, *16*, 7745; c) W. Ma, Y. Gao, L. Shang, W. Zhou, N. Yao, L. Jiang, Q. Qiu, J. Li, Y. Shi, Z. Hu, Z. Huang, *Adv. Sci.* **2022**, *9*, 2103873.

[8] H. Yang, L. Pan, X. Wang, H.-X. Deng, M. Zhong, Z. Zhou, Z. Lou, G. Shen, Z. Wei, *Adv. Funct. Mater.* **2019**, *29*, 1904416.

[9] Y. Cui, Z. Zhou, X. Wang, X. Wang, Z. Ren, L. Pan, J. Yang, *Nano Res.* **2021**, *14*, 2224.

[10] a) B. A. Unlu, A. Karatay, E. Avcı, E. A. Yildiz, A. Ates, A. Elmali, *J. Lumin.* **2022**, *248*, 118987; b) S. Pal, D. N. Bose, *Solid State Commun.* **1996**, *97*, 725; c) Y. Liao, H. Liu, G. Yuan, Z. Huang, X. Qi, *Cryst. Res. Technol.* **2020**, *55*, 2000102; d) V. Sowjanya, K. V. Bangera, G. K. Shivakumar, *Superlattice. Microstruct.* **2019**, *129*, 220; e) S. A. Hussein, *Cryst. Res. Technol.* **1989**, *24*, 635; f) J. Shang, L. Pan, X. Wang, J. Li, H.-X. Deng, Z. Wei, *J. Mater. Chem. C* **2018**, *6*, 7201; g) M. A. S. Touskia, M. Hosseini, *Physica E* **2020**, *118*, 113875.

[11] a) T. Chattopadhyay, R. P. Santandrea, H. G. V. Schnering, *J. Phys. Chem. Solids* **1985**, *46*, 351; b) S. Sun, B. Zhang, X. Wang, W. Zhang, *APL Mater.* **2021**, *9*, 121105.

[12] T. Zhang, J. Wang, P. Wu, A.-Y. Lu, J. Kong, *Nat. Rev. Mater.* **2023**, *8*, 799.

[13] M. Parlak, C. Ercelebi, I. Günal, H. Özkan, N. M. Gasanly, *Cryst. Res. Technol.* **1996**, *31*, 673.

[14] A. M. Aliev, M. A. Nizametdinova, V. Y. Steinshreiber, *Phys. Status Solidi B* **1981**, *107*, K151.

[15] S. Misra, P. Levinský, A. Dauscher, G. Medjahdi, J. Hejtmánek, B. Malaman, G. J. Snyder, B. Lenoir, C. Candolfi, *J. Mater. Chem. C* **2021**, *9*, 5250.

[16] V. Rajaji, K. Pal, S. C. Sarma, B. Joseph, S. C. Peter, U. V. Waghmare, C. Narayana, *Phy. Rev. B* **2018**, *97*, 155158.

[17] a) A. K. Tkalich, V. N. Demin, V. P. Zlomanov, *J. Solid State Chem.* **1995**, *116*, 33; b) C. Liu, Y. Yuan, X. Zhang, J. Su, X. Song, H. Ling, Y. Liao, H. Zhang, Y. Zheng, J. Li, *Nanomaterials* **2020**, *10*, 1887.

[18] M. A. Nizametdinova, *Phys. Status Solidi B* **1980**, *97*, K9.

[19] S. Misra, C. Barreteau, J.-C. Crivello, V. M. Giordano, J.-P. Castellan, Y. Sidis, P. Levinský, J. Hejtmánek, B. Malaman, A. Dauscher, B. Lenoir, C. Candolfi, S. Pailhès, *Phys. Rev. Res.* **2020**, *2*, 043371.

[20] Y. Wang, D. C. Alsmeyer, R. L. McCreery, *Chem. Mater.* **1990**, *2*, 557.

[21] A. V. Bandura, A. V. Kovalenko, D. D. Kuruch, R. A. Evarestov, *Eur. J. Inorg. Chem.* **2021**, *2021*, 126.

[22] S. Yang, C. Hu, M. Wu, W. Shen, S. Tongay, K. Wu, B. Wei, Z. Sun, C. Jiang, L. Huang, Z. Wang, *ACS Nano* **2018**, *12*, 8798.

[23] a) O. Makkawi, Y. Qiu, W. Feng, P. A. Hu, *J. Nanosci. Nanotechnol.* **2016**, *16*, 9813; b) Z. Yang, W. Jie, C.-H. Mak, S. Lin, H. Lin, X. Yang, F. Yan, S. P. Lau, J. Hao, *ACS Nano* **2017**, *11*, 4225.

[24] Z. Sun, Z. Guo, D. Yan, P. Cheng, L. Chen, Y. Shi, Y. Huang, Z. Wang, K. Wu, B. Feng, *Phys. Rev. Mater.* **2023**, *7*, 094004.

[25] a) H. G. Rosa, J. Lu, L. C. Gomes, M. J. L. F. Rodrigues, S. C. Haur, J. C. Gomes, *Adv. Opt. Mater.* **2018**, *6*, 1701327; b) R. Hristu, S. G. Stanciu, D. E. Tranca, E. K. Polychroniadis, G. A. Stanciu, *Sci. Rep.* **2017**, *7*, 4870; c) C.-J. Kim, L. Brown, M. W. Graham, R. Hovden, R. W. Havener, P. L. McEuen, D. A. Muller, J. Park, *Nano Lett.* **2013**, *13*, 5660. d) F. Xia, F. Wang, H. Hu, X. Xu, Y. Li, T. Zhai, *J. Inorg. Mater.* **2021**, *10*, 1022.

[26] J. Zhang, W. Zhao, P. Yu, G. Yang, Z. Liu, *2D Mater.* **2020**, *7*, 042002.

[27] X. Zhou, J. Cheng, Y. Zhou, T. Cao, H. Hong, Z. Liao, S. Wu, H. Peng, K. Liu, D. Yu, *J. Am. Chem. Soc.* **2015**, *137*, 7994.

[28] S. Pal, D. N. Bose, S. Asokan, E. S. R. Gopal, *Solid State Commun.* **1991**, *80*, 753.

[29] a) Y. Gu, H. Cai, J. Dong, Y. Yu, A. N. Hoffman, C. Liu, A. D. Oyedele, Y. C. Lin, Z. Ge, A. A. Puretzky, G. Duscher, M. F. Chisholm, P. D. Rack, C. M. Rouleau, Z. Gai, X. Meng, F. Ding, D. B. Geohegan, K. Xiao, *Adv. Mater.* **2020**, *32*, 1906238; b) M. Zhong, H. Meng, S. Liu, H. Yang, W. Shen, C. Hu, J. Yang, Z. Ren, B. Li, Y. Liu, J. He, Q. Xia, J. Li, Z. Wei, *ACS Nano* **2020**, *15*, 1701.

[30] N. Zhou, Z. Zhang, F. Wang, J. Li, X. Xu, H. Li, S. Ding, J. Liu, X. Li, Y. Xie, R. Yan, Y. Ma, T. Zhai, *Adv. Sci.* **2022**, *9*, 2202177.

[31] a) Z.-Y. Chen, M. Xiong, Z.-Y. Zeng, X.-R. Chen, Q.-F. Chen, *Solid State Commun.* **2021**, *326*, 114163; b) Y. Xu, T. Liu, K. Liu, Y. Zhao, L. Liu, P. Li, A. Nie, L. Liu, J. Yu, X. Feng, F. Zhuge, H. Li, X. Wang, T. Zhai, *Nat. Mater.* **2023**, *22*, 1078.

[32] a) C. Xie, C. Mak, X. Tao, F. Yan, *Adv. Funct. Mater.* **2017**, *27*, 1603886; b) J. Jiang, T. Xu, J. Lu, L. Sun, Z. Ni, *Research* **2019**, *2019*, 4641739; c) D. H. Kang, M. S. Kim, J. Shim, J. Jeon, H. Y. Park, W. S. Jung, H. Y. Yu, C. H. Pang, S. Lee, J. H. Park, *Adv. Funct. Mater.* **2015**, *25*, 4219; d) O. Lopez-Sanchez, D. Lembke, M. Kayci, A. Radenovic, A. Kis, *Nat.*

[33] G. Kremer, A. Mahmoudi, M. Bouaziz, C. Brochard-Richard, L. Khalil, D. Pierucci, F. Bertran, P. L. Fèvre, M. G. Silly, J. Chaste, F. Oehler, M. Pala, F. Bisti, A. Ouerghi, *Phy. Rev. Mater.* **2023**, *7*, 074601.

[34] B. Radisavljevic, A. Kis, *Nat. Mater.* **2013**, *12*, 815.

[35] R. Duan, Y. He, C. Zhu, X. Wang, C. Zhu, X. Zhao, Z. Zhang, Q. Zeng, Y. Deng, M. Xu, Z. Liu, *Adv. Funct. Mater.* **2022**, *32*, 2113255.

[36] F. Xia, H. Wang, Y. Jia, *Nat. Commun.* **2014**, *5*, 4458.

[37] A. Parisini, A. Bosio, H. J. von Bardeleben, J. Jimenez, S. Dadgostar, M. Pavesi, A. Baraldi, S. Vantaggio, *Mater. Sci. Semicond. Process.* **2022**, *138*, 106307.

[38] a) N. Zhou, L. Gan, R. Yang, F. Wang, L. Li, Y. Chen, D. Li, T. Zhai, *ACS Nano* **2019**, *13*, 6297; b) F. Wang, J. Wu, Y. Zhang, S. Yang, N. Zhang, H. Li, T. Zhai, *Sci. China Mater.* **2022**, *65*, 451.

[39] a) Z. Wang, P. Wang, F. Wang, J. Ye, T. He, F. Wu, M. Peng, P. Wu, Y. Chen, F. Zhong, R. Xie, Z. Cui, L. Shen, Q. Zhang, L. Gu, M. Luo, Y. Wang, H. Chen, P. Zhou, A. Pan, X. Zhou, L. Zhang, W. Hu, *Adv. Funct. Mater.* **2020**, *30*, 1907945; b) W. Yang, J. Yang, K. Zhao, Q. Gao, L. Liu, Z. Zhou, S. Hou, X. Wang, G. Shen, X. Pang, Q. Xu, Z. Wei, *Adv. Sci.* **2021**, *8*, 2100075.

[40] a) W. Zeng, J. Li, L. Feng, H. Pan, X. Zhang, H. Sun, Z. Liu, *Adv. Funct. Mater.* **2019**, *29*, 1900129; b) B. Tan, Y. Wu, F. Gao, H. Yang, Y. Hu, H. Shang, X. Zhang, J. Zhang, Z. Li, Y. Fu, D. Jia, Y. Zhou, H. Xiao, P. Hu, *ACS Appl. Mater. Interfaces* **2022**, *14*, 16453.

[41] a) F. Wang, Z. Zhang, Y. Zhang, A. Nie, W. Zhao, D. Wang, F. Huang, T. Zhai, *Adv. Mater.* **2020**, *32*, 2001979; b) Q. Liang, Q. Wang, Q. Zhang, J. Wei, S. X. Lim, R. Zhu, J. Hu, W. Wei, C. Lee, C. Sow, W. Zhang, A. T. S. Wee, *Adv. Mater.* **2019**, *31*, 1807609.

[42] S. Li, Y. Zhang, W. Yang, H. Liu, X. Fang, *Adv. Mater.* **2020**, *32*, 1905443.

[43] X. Y. Liu, S. Y. Li, Z. Q. Li, F. Cao, L. Su, D. V. Shtansky, X. S. Fang, *ACS Appl. Mater. Interfaces* **2022**, *14*, 48936.

[44] a) X. Zhou, L. Gan, W. Tian, Q. Zhang, S. Jin, H. Li, Y. Bando, D. Golberg, T. Zhai, *Adv. Mater.* **2015**, *27*, 8035; b) X. Zhou, Q. Zhang, L. Gan, X. Li, H. Li, Y. Zhang, D. Golberg, T. Zhai, *Adv. Funct. Mater.* **2016**, *26*, 704; c) F. Wang, T. Gao, Q. Zhang, Z. Y. Hu, B. Jin, L. Li, X. Zhou, H. Li, G. Van Tendeloo, T. Zhai, *Adv. Mater.* **2019**, *31*, 1806306.

[45] X. Gong, M. Tong, Y. Xia, W. Cai, J. S. Moon, Y. Cao, G. Yu, C.-L. Shieh, B. Nilsson, A. J. Heeger, *Science* **2009**, *325*, 1665.

[46] a) M. Amani, C. Tan, G. Zhang, C. Zhao, J. Bullock, X. Song, H. Kim, V. R. Shrestha, Y. Gao, K. B. Crozier, M. Scott, A. Javey, *ACS Nano* **2018**, *12*, 7253; b) Y. Wang, P. Wu, Z. Wang, M. Luo, F. Zhong, X. Ge, K. Zhang, M. Peng, Y. Ye, Q. Li, H. Ge, J. Ye, T. He, Y. Chen, T. Xu, C. Yu, Y. Wang, Z. Hu, X. Zhou, C. Shan, M. Long, P. Wang, P. Zhou, W. Hu, *Adv. Mater.* **2020**, *32*, 2005037.

[47] J. Misiewicz, *J. Phys. Condens. Matter* **1990**, *2*, 2053.

[48] N. Zuo, A. Nie, C. Hu, W. Shen, B. Jin, X. Hu, Z. Liu, X. Zhou, T. Zhai, *Small* **2021**, *17*, 2008078.

[49] Z. Zhou, M. Long, L. Pan, X. Wang, M. Zhong, M. Blei, J. Wang, J. Fang, S. Tongay, W. Hu, J. Li, Z. Wei, *ACS Nano* **2018**, *12*, 12416.